Determination of mean inner potential of germanium using off-axis electron holography

Jing Li,[a]* M. R. McCartney,[b] R. E. Dunin-Borkowski[b] and David J. Smith[a]

[a]*Department of Physics and Astronomy, Arizona State University, Tempe, AZ 85287-1504, USA, and* [b]*Center for Solid State Science, Arizona State University, Tempe, AZ 85287-1704, USA. E-mail: jing.li@asu.edu*

Abstract

Off-axis electron holography has been used to determine the mean inner potential of germanium using cleaved 90° wedge samples, where the wedge thickness profiles were checked by weak-beam dark-field extinction fringes. Dynamical contributions to the phase of the image were minimized by tilting to weakly diffracting conditions, as confirmed by reference to convergent-beam electron diffraction patterns. Small residual corrections were determined using multislice calculations. From a total of 18 separate measurements, it is concluded that the value of the mean inner potential is 14.3 (2) V, which agrees with recent theoretical calculations to within experimental error.

1. Introduction

The mean inner potential, V_o, is the volume-averaged electrostatic part of the crystal potential (Bethe, 1928). It is proportional to the diamagnetic susceptibility (Rosenfeld, 1929) and its value is very sensitive to variations in charge density associated with bonding and ionicity in crystalline materials (O'Keeffe & Spence, 1994). Theoretical calculations of V_o based on the neutral-atom scattering factors of Doyle & Turner (1968) provide an upper bound for V_o, whereas a lower limit can be obtained from calculations based on the ionized-free-atom bonding model of Radi (1970). The true value, which depends on the degree of ionicity of the material, must lie somewhere in between these two limits. In practice, the mean inner potential is important in applications such as reflection high-energy electron diffraction (RHEED) (Peng *et al.*, 1998), low-energy electron diffraction, Fresnel imaging of interfaces (Ross & Stobbs, 1991) and electron holography (Weiss *et al.*, 1993). For example, an accurate knowledge of V_o is required when analyzing RHEED patterns to determine crystal ionicity (Peng *et al.*, 1997).

In the transmission electron microscope (TEM), the phase change of an electron wave passing through the sample relative to a wave that has only passed through vacuum is sensitive to changes of the specimen thickness and V_o. Once the value of V_o has been accurately determined, then small variations of the sample thickness can be quantified using electron holography,

leading to useful applications such as the measurement of surface steps and the sizes of nanoparticles. We are particularly interested in using this technique to determine the potential distribution across doped or biased semiconductor junctions (McCartney *et al.*, 1994), and thus reliable information about V_o in the absence of dopants and biasing effects is required.

Only limited experimental data for V_o are so far available (Spence, 1993; Gajdardziska-Josifovska & Carim, 1999). Most methods for the measurement of V_o have relative errors reported to be in the range of 2.5 to 10%, but results from different groups and different techniques differ by even larger amounts, suggesting the presence of systematic errors. In a recent study of cleaved wedge samples (Gajdardziska-Josifovska *et al.*, 1993), it was shown that the use of off-axis electron holography when combined with digital recording could give a factor of 3 improvement in the precision of V_o values relative to earlier studies. In this study, we have used the same approach to measure the mean inner potential of germanium, again paying particular attention to the accurate measurement of critical experimental parameters such as magnification, crystal tilt and specimen thickness, as well as to the minimization of dynamical diffraction effects.

2. Experimental

2.1. Sample and microscope

The Ge samples used in this study were 90° wedges, cleaved from a ⟨100⟩ wafer and mounted onto copper
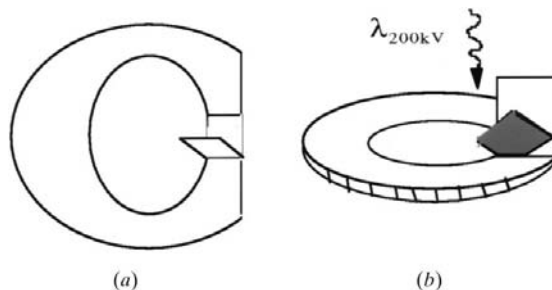

Fig. 1. Illustration of wedge sample mounting geometry: (*a*) cutting and bending of circular Cu grid viewed at oblique angle; (*b*) cleaved wedge glued to grid within microscope.

grids. Figs. 1(*a*) and 1(*b*) illustrate the shape of the grid and the sample-mounting geometry. Off-axis electron holograms were recorded using a Philips CM200 field-emission-gun (FEG) TEM. This instrument has a high-coherence field-emission electron source and an electrostatic biprism mounted in the selected-area aperture holder. A positive voltage applied to the biprism causes interference of the specimen wave with the vacuum reference wave. The microscope is also equipped with a strong (Lorentz) mini-lens beneath the bottom bore of the objective-lens pole piece. This mini-lens is normally used for field-free imaging of magnetic materials in place of the usual objective lens. In the current experiments, it proved very useful by providing enlarged fields of view. With a biprism voltage in the range of 100 to 110 V, the contrast of the interference fringes [defined as $(I_{max} - I_{min})/2I_{mean}$] was typically ~15–20% using the Lorentz mode, the fringe spacing was ~3.5–4.0 nm and the region of fringe overlap was ~500 nm in width. The microscope is equipped with a 1024 × 1024 Gatan 792 multiscan CCD camera for digital recording. The fixed position of this camera relative to the microscope imaging system permits convenient recording of reference holograms, which are essential for correcting phase distortions associated with the illumination and imaging systems (de Ruijter & Weiss, 1993).

2.2. *Measurement of wedge angle*

Our experience with crystal cleavage suggests that the cleavage angle of Ge wedge samples is not often 90°; using (100) Ge samples, perhaps only about 10% cleaved uniformly on both {110} planes. Indeed, we suspect that variations in wedge angle are the most likely cause of the large spread in values that have been reported for the mean inner potential of silicon as
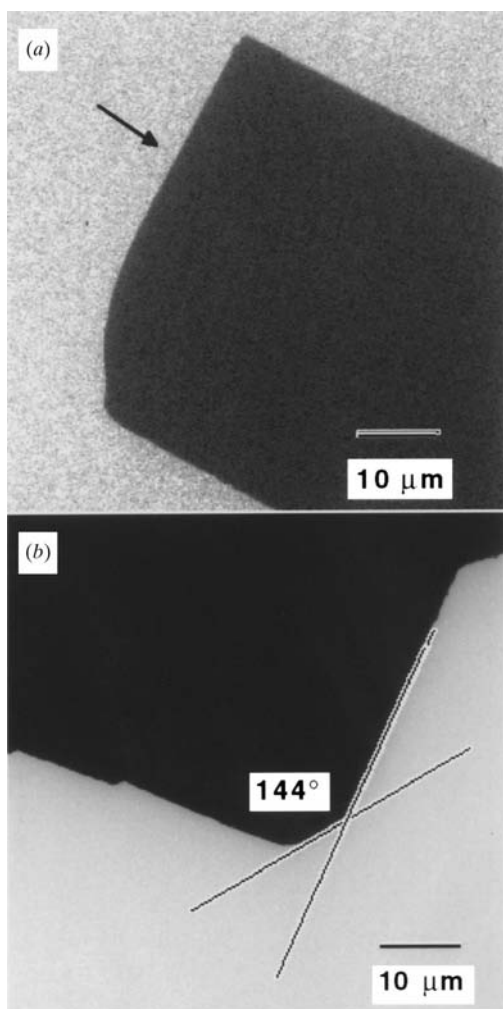

Fig. 2. (*a*) Wedge of cleaved silicon viewed from [001] direction recorded at 290× magnification. Hologram would normally be recorded from region arrowed. (*b*) Wedge viewed from the [100] direction after rotation by 90°. Tip of wedge does not show the expected 90° angle between ⟨110⟩ planes.
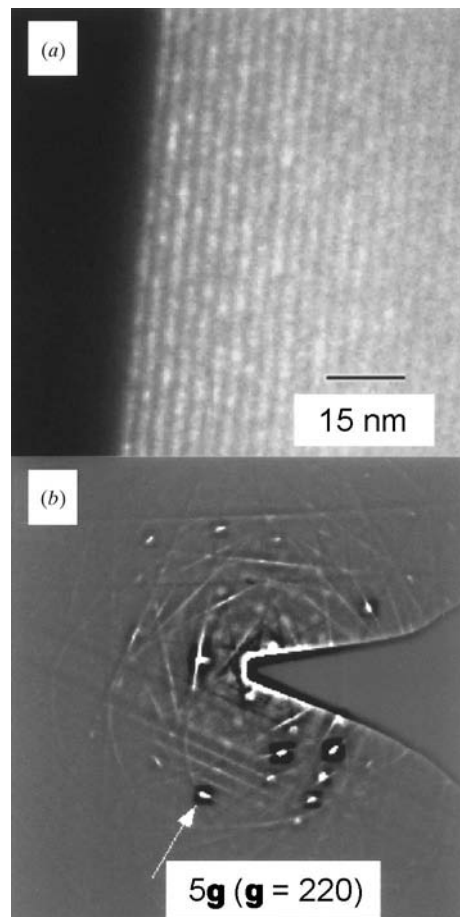

Fig. 3. (*a*) Part of WBDF image from 90° Ge wedge satisfying 5**g** reflection, showing periodic thickness extinction fringes; (*b*) corresponding selected-area electron diffraction pattern used to determine imaging conditions.

determined by off-axis electron holography (Gajdard-ziska-Josifovska *et al.*, 1993; Wang *et al.*, 1997; Rau, 1998). Fig. 2 emphasizes this point in the form of low-magnification images of a silicon ⟨100⟩ cleaved wedge sample viewed from directions both perpendicular and parallel to the thin cleaved edge. The arrow in Fig. 2(*a*) indicates the thin edge of the sample. While the appearance of Fig. 2(*a*) is consistent with the image of a wedge angle of 90°, the flat surface visible in Fig. 2(*b*) after rotation of the sample out of the plane by 90° indicates that the thin edge actually cleaved along an unknown plane, giving a wedge angle of close to 144°. This possibility of irregular crystal cleavage reinforces the need for an independent measurement of crystal thickness.

A common electron-microscope method for determining crystal thickness is based on the weak-beam dark-field (WBDF) imaging technique (Hirsch *et al.*, 1977). For a crystal tilted to satisfy a (**g**, *n***g**) dark-field condition, the thickness change of the sample, d*t*/d*x*, is given by the expression

$$dt/dx = 1/ds, \qquad (1)$$

where *d* is the spacing of the WB thickness extinction fringes, as measured from the DF image. The excitation errors are determined from the expression

$$s = \tfrac{1}{2}(n-1)|g|^2\lambda, \qquad (2)$$

where λ is the wavelength of the incident electron wave and *n* corresponds to the order of the beam intersected by the Ewald sphere (Williams & Carter, 1996). Note that *n* is not necessarily an integer.

Fig. 3 shows an experimental (**g**, 5**g**) WBDF image [where **g** ≡ (220)] and the corresponding selected-area electron diffraction pattern. The measured mean fringe spacing is 3.80 nm and the value of *n* is estimated to be ~5 ± 0.1 from the diffraction pattern. The second column of Table 1 shows the expected rate of change of thickness calculated from (1) for slightly different values of *n* as shown in the first column. For comparison, the values of d*t*/d*x* shown in column 4 are those expected for the small range of different wedge angles as shown in column 3. The numbers shown in bold indicate that, to within experimental error, our measured weak-beam thickness fringes are consistent with a wedge angle of 90°.
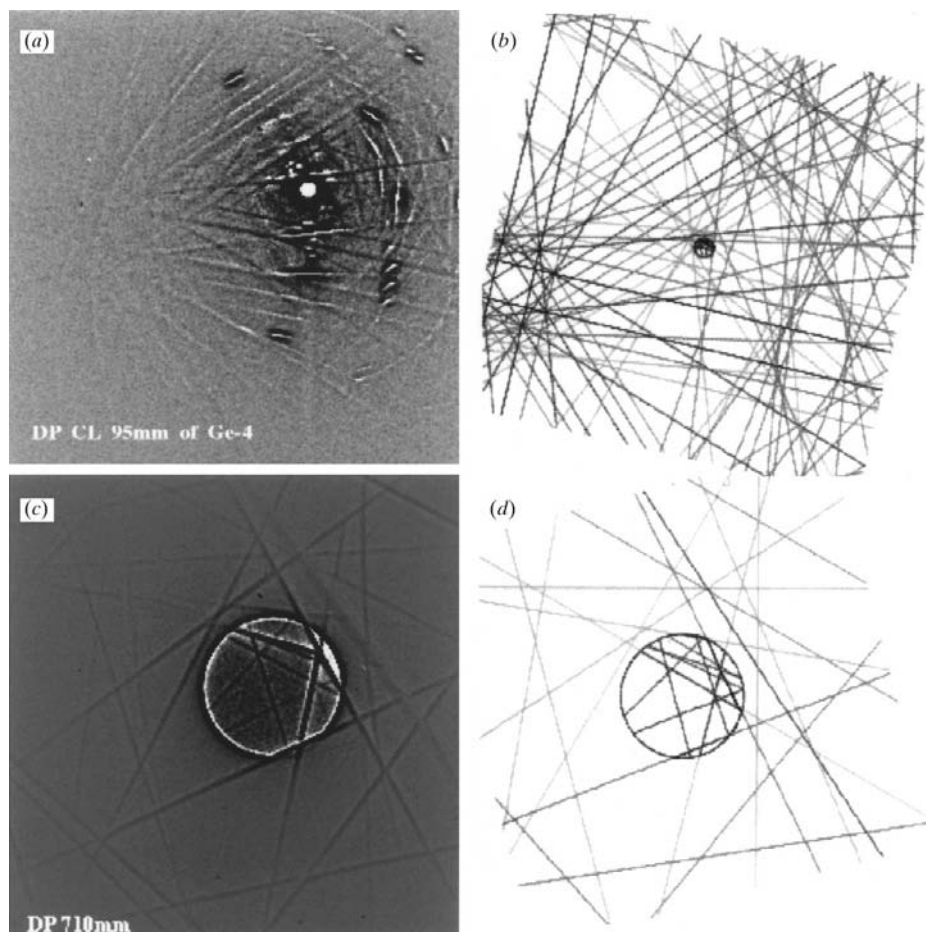

Fig. 4. Comparison of experimental and simulated CBED patterns: (*a*) experimental pattern taken at short camera length of 95 mm; (*b*) simulated pattern; (*c*) experimental pattern taken at camera length of 710 mm; (*d*) simulated pattern.

Table 1. *Weak-beam measurements used to determine wedge cleavage angles*

Data in column 2 are calculated from equations (1) and (2) using measurements of experimental WB contours. Data in column 4 show expected dt/dx values based on wedge angles in column 3. Correspondence of numbers shown in bold confirm the 90° wedge angle (see text).

$n\mathbf{g}$ (5.0 < n < 5.1) condition	dt/dx from WB fringes	Wedge angle (°)	dt/dx from wedge angle
5.10	2.050	89	2.041
5.09	2.056	89.2	2.048
5.08	2.060	89.4	2.056
5.07	2.066	89.6	2.063
5.06	**2.071**	89.8	2.071
5.05	**2.076**	**90**	**2.078**
5.04	**2.081**	90.2	2.086
5.03	2.086	90.4	2.093
5.02	2.091	90.6	2.101
5.01	2.096	90.8	2.108
5.00	2.102	91	2.116

2.3. *Experimental conditions for holography*

Samples were routinely tilted away from the exact zone-axis orientation in order to avoid strong dynamical diffraction when recording the off-axis electron holograms. Convergent-beam electron diffraction (CBED) patterns were recorded at several different camera lengths so that the precise orientation of the sample could be determined. By careful comparison of experimental and simulated CBED patterns, tilting angles could be determined to an accuracy of better than 0.05°. Fig. 4 shows an example of a comparison between experimental and simulated CBED patterns used in this study.

2.4. *Mode of operation*

Fig. 5(*a*) shows a typical hologram taken in the Lorentz operating mode at an indicated microscope magnification of 35K×, while Fig. 5(*b*) shows a hologram taken in the normal imaging mode at a magnification of 400K×. The field of view in the Lorentz mode is several hundred nanometres, whereas a region that only extends for about 30 nm into the sample is visible in the normal mode. The larger field of view in the former geometry decreases the possibility that imperfections or local irregularities in the thinnest region of the sample may affect the final result. For example, the amorphous or disordered material along the edge of the sample in Fig. 5(*b*) would have a strong influence on the phase profile in this region. In the Lorentz mode, the effect of this amorphous material on the change of the phase would be much less serious since a larger area of specimen away from the edge is sampled. It is also worth noting that the greater size of the sampling area enhances the accuracy with which the phase profile can be determined. In our experiments, we used both modes to record holograms and the calculated V_o values were

consistent for each mode. However, the spread of values was considerably less for the Lorentz mode.

3. Results and discussion

3.1. *Measurement of V_o*

In the absence of dynamical diffraction effects, and ignoring any magnetic and other electrostatic potentials associated with the sample, the phase change Φ of the electron wave passing through the specimen can be written (Reimer, 1989) as

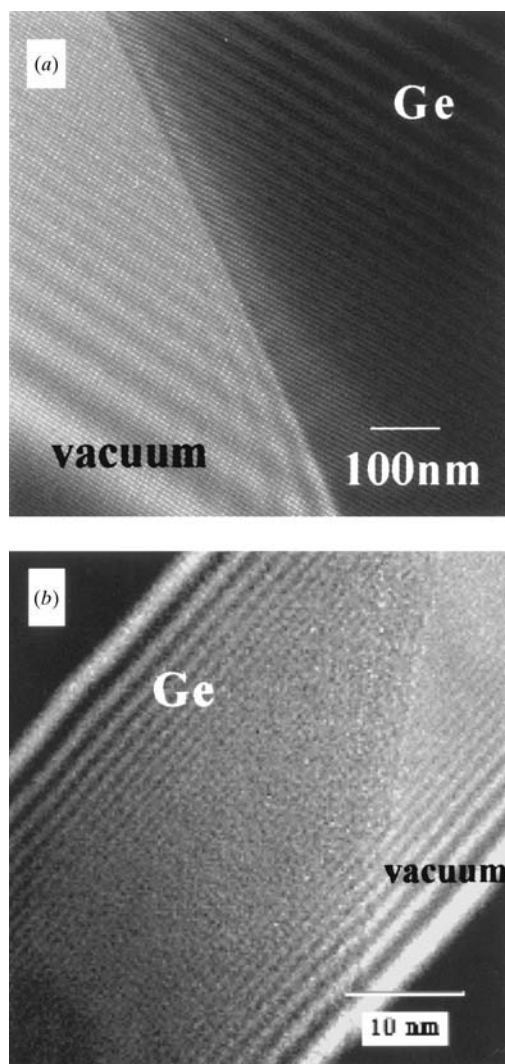$$\Phi = \frac{2\pi e}{\lambda E}\frac{E_0 + E}{2E_0 + E}|V_o|t = C_E|V_o|t, \qquad (3)$$

Fig. 5. (*a*) Off-axis electron hologram of Ge wedge recorded in Lorentz imaging mode at 35K× magnification; (*b*) off-axis electron hologram recorded in conventional imaging mode at magnification of 400K×. Width of field of view limited to ~50 nm.

where C_E is an energy-dependent parameter [$C_E = 0.00728$ rad (V nm)$^{-1}$ when the electron energy E is 0.20 MeV], E_o is the rest-mass energy of the electron (in MeV) and t is the specimen thickness.

For a sample of uniform V_o and a known wedge angle, it is convenient to rearrange equation (1) and differentiate, giving an expression that enables V_o to be calculated:

$$V_0 = \frac{1}{C_E} \frac{d\Phi/dx}{dt/dx}. \qquad (4)$$

The change in phase with position on the sample, $d\Phi/dx$, can be determined after reconstruction of an off-axis electron hologram to obtain the complex image wave (Lichte, 1991). Digital recording and phase averaging allow high accuracy in the phase determination (de Ruijter & Weiss, 1993): it is thus essential that the magnification and the lateral rate of thickness change, dt/dx, are calibrated as accurately as possible. Ge lattice fringes were used for calibration in normal mode operation and a catalase standard was used in the Lorentz mode. For a cubic crystal cleaved along orthogonal $\langle 110 \rangle$ planes, the wedge angle is 90° and the factor dt/dx is 2 when the electron beam is incident along the [001] zone axis. Slight corrections are, however, required when the sample is tilted away from the exact zone axis to avoid dynamical diffraction.

The phase image reconstructed from Fig. 5(*a*) is displayed as an equiphase pseudocontour image in Fig. 6. The 2π phase contours are straight, parallel to the edge and uniformly spaced over a large area, implying a uniform wedge angle. Fig. 7(*a*) shows the averaged phase and amplitude profiles taken from the reconstructed Lorentz-mode hologram after phase unwrapping. The area used for averaging is indicated by the box
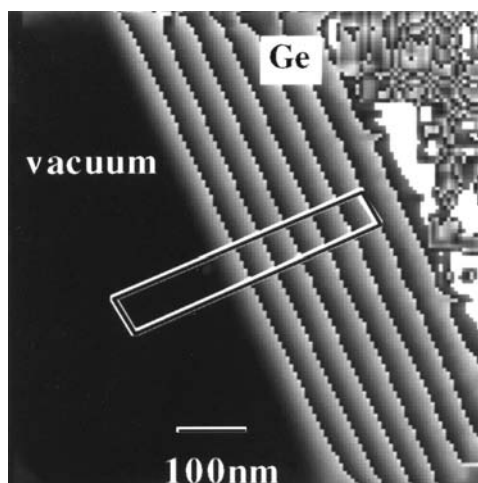
in Fig. 6. Fig. 7(*b*) shows profiles taken from a reconstructed normal mode hologram. The smoothness of the phase profiles with increasing thickness serves to confirm the high quality of the holographic recording and reconstruction process, as well as the high degree of flatness of the cleavage planes. It is clear from both amplitude profiles that the amplitude decreases smoothly at greater crystal thicknesses, which is a good indication that dynamical diffraction effects are weak.

3.2. Thickness correction

The cleaved Ge wedges were always tilted away from the exact [100] zone axis, in order to minimize any systematic and non-systematic interactions that might affect the experimental determination of V_o. Several different (mis)orientations were used. However, a slight change in the projected crystal thickness then occurs, which must be taken into account. The corresponding geometrical correction to dt/dx in equation (2) is given by
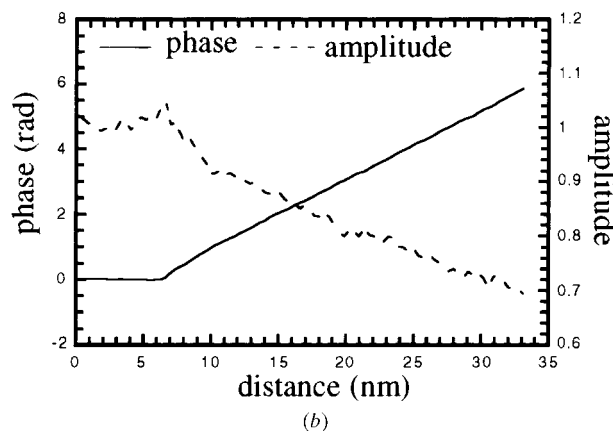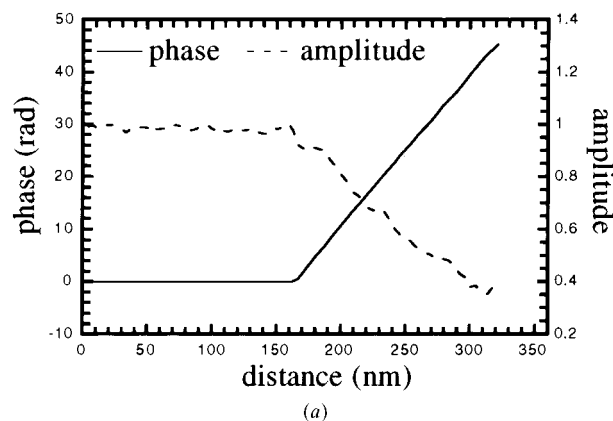

(*a*)

Fig. 6. Phase image of Ge wedge reconstructed from Fig. 5(*a*). Phase contours of 2π rad. Region at upper right was not unwrapped owing to poor signal-to-noise ratio in thick crystal.

(*b*)

Fig. 7. (*a*) Averaged phase and amplitude profiles taken from boxed region indicated in Fig. 6; (*b*) Averaged phase and amplitude profiles for image wave reconstructed from normal-mode hologram. Note change in horizontal length scale.

Table 2. *Examples of V_o values before and after dynamical correction for several tilting geometries*

	Ge-1 normal mode	Ge-2 Lorentz mode	Ge-3 Lorentz mode	Ge-4 Lorentz mode
Tilt angles				
α (°)	4.915	9.03	4.72	9.08
β (°)	1.74	1.875	2.065	1.51
V_o before correction (V)	14.34	14.09	14.23	14.17
Dynamical correction (V)	0.108	0.197	0.088	0.155
V_o after correction (V)	14.44	14.29	14.32	14.33

$$\frac{dt}{dx} = \frac{\tan(45 + \alpha) + \tan(45 - \alpha)}{\cos(\beta)}, \quad (5)$$

where α and β are the tilting angles defined by the sketch shown in Fig. 8 (Gajdardziska-Josifovska *et al.*, 1993).

3.3. *Dynamical corrections*

In order to account for residual dynamical diffraction effects, atomistic simulations of the amplitude and phase, which included the V_o term, were performed using multislice calculations (Dunin-Borkowski, 1999). Table 2 shows a summary of the results for several different crystal tilts, together with the dynamical corrections, which were usually quite small (~1–2%). The measurements in the normal mode were consistent with these measurements, which were made in the Lorentz mode. Fig. 9 summarizes all of our results for multiple Ge wedges and different tilting angles in the form of a bar chart. From these measurements, it can be concluded that the mean inner potential of germanium is 14.3 (2) V.

3.4. *Comparison with other work*

The only experimental determination of the mean inner potential of germanium so far reported involved the use of thin-film interferometry, with a result of 15.6 (8) V (Hoffmann & Jönsson, 1965). Theoretical estimates of the upper and lower limits on the V_o value for germanium have also been reported (Gajdardziska-Josifovska & Carim, 1999). A calculation based on the scattering factors for ionized atoms (Radi, 1970) set a lower limit for V_o of 13.69 V. Neutral-atom scattering factors (Doyle & Turner, 1968) set an upper limit for V_o of 15.59 V. In a recent theoretical study, the full potential linearized augmented plane-wave (FLAPW) method was used to take full account of the electron-bonding distribution within a thin slab of Ge (Kim *et al.*, 1998). A value of 14.12 (3) V was calculated for a ⟨111⟩-oriented Ge slab, which agrees closely with our experimental determination. Finally, it is perhaps of interest to mention that the reported V_o measured by electron holography for GaAs was 14.5 V (Gajdardziska-Josifovska *et al.*, 1993), which is a little higher that that found here for Ge: owing to its greater ionicity, GaAs
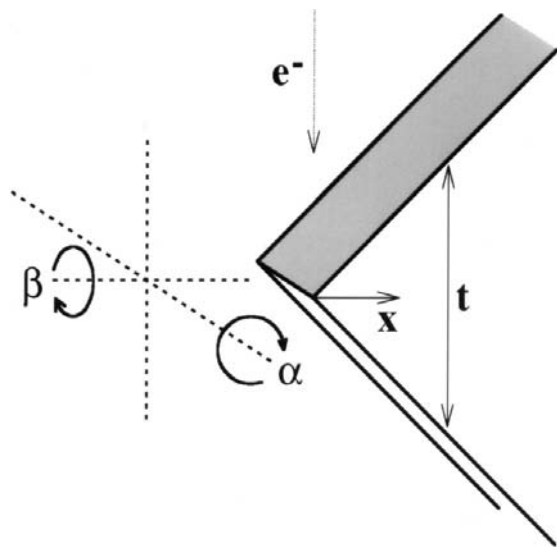

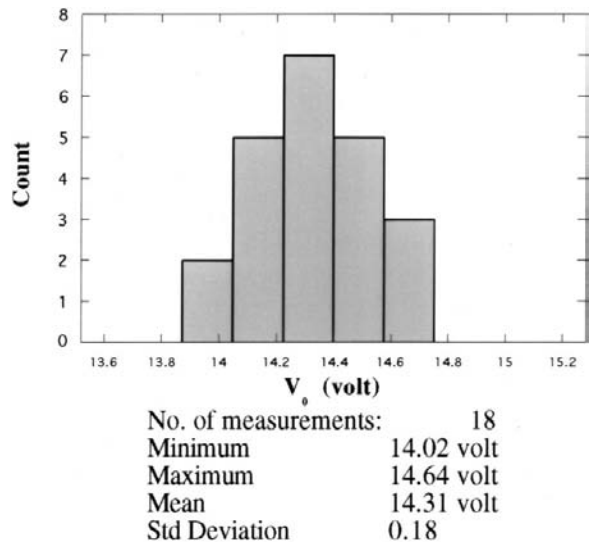Fig. 8. Schematic showing sample dimensions and tilting geometry.

No. of measurements: 18
Minimum 14.02 volt
Maximum 14.64 volt
Mean 14.31 volt
Std Deviation 0.18

Fig. 9. Bar chart showing range of V_o values measured using Lorentz and normal imaging mode.

would normally be expected to have slightly lower V_o than Ge.

4. Conclusions

Using off-axis electron holography, the bulk mean inner potential of crystalline Ge was determined experimentally to be 14.3 (2) V. This value is within the calculated upper and lower theoretical limits and very close to a recent theoretical determination that took charge redistribution into account. Measurements based on several confirmed 90° wedge samples using the Lorentz imaging mode of the microscope displayed a small spread ($<3\%$) of calculated values. Our approach should thus have sufficient sensitivity for investigating problems such as the effect of composition in Ge/Si alloys on the mean inner potential.

References

Bethe, H. A. (1928). *Ann. Phys. (Leipzig)*, **87**, 55–128.
Doyle, P. & Turner, P. S. (1968). *Acta Cryst.* A**24**, 390–397.
Dunin-Borkowski, R. E. (1999). In preparation.
Gajdardziska-Josifovska, M. & Carim, H. (1999). *Introduction to Electron Holography*, edited by E. Völkl, L. Allard & D. C. Joy, ch. 12. New York: Springer.
Gajdardziska-Josifovska, M., McCartney, M. R., de Ruijter, W. J., Smith, D. J., Weiss, J. K. & Andzuo, J. M. (1993). *Ultramicroscopy*, **53**, 285–299.
Hirsch, P. B., Howie, A., Nicholson, R. N., Pashley, D. W. & Whelan, M. J. (1977). *Electron Microscopy of Thin Crystals*. Malabar: Krieger.
Hoffmann, H. & Jönsson, C. (1965). *Z. Phys.* **182**, 360–365.
Kim, M. Y., Zuo, J. M. & Spence, J. C. H. (1998). *Phys. Status Solidi A*, **166**, 445–451.
Lichte, H. (1991). *Adv. Opt. Electron Microsc.* **12**, 25.
McCartney, M. R., Smith, D. J., Hull, R., Bean, J. C., Voelkl, E. & Frost, B. (1994). *Appl. Phys. Lett.* **65**, 2603–2605.
O'Keeffe, M. & Spence, J. C. H. (1994). *Acta Cryst.* A**50**, 33–45.
Peng, L.-M., Dudarev, S. L. & Whelan, M. J. (1997). *Phys. Rev. B*, **56**, 314–319.
Peng, L.-M., Dudarev, S. L. & Whelan, M. J. (1998). *Phys. Rev. B*, **57**, 7259–7265.
Radi, G. (1970). *Acta Cryst.* A**26**, 41–59.
Rau, W.-D. (1998). Private communication.
Reimer, L. (1989). *Transmission Electron Microscopy*, p. 57. Berlin: Springer.
Rosenfeld, L. (1929). *Naturwissenschaften*, **17**, 49–50.
Ross, F. & Stobbs, W. M. (1991). *Philos. Mag.* A**63**, 1–35.
Ruijter, W. J. de & Weiss, J. K. (1993). *Ultramicroscopy*, **50**, 269–283.
Spence, J. C. H. (1993). *Acta Cryst.* A**49**, 231–260.
Wang, Y. C., Chou, T. M., Libera, M. & Kelly, T. F. (1997). *Appl. Phys. Lett.* **70**, 1296–1298.
Weiss, J. K., de Ruijter, W. J., Gajdardziska-Josifovskja, M., McCartney, M. R. & Smith, D. J. (1993). *Ultramicroscopy*, **50**, 301–311.
Williams, D. B. & Carter, C. B. (1996). *Transmission Electron Microscopy III*, pp. 423–425. New York: Plenum.